

An Assessment of Milling Time on the Structure and Properties of a Nanostructured Ferritic Alloy (NFA)

RICHARD DIDOMIZIO, SHENYAN HUANG, LAURA DIAL, JAN ILAVSKY,
and MIKE LARSEN

The tensile properties of a 14 wt pct chromium nanostructured ferritic alloy (NFA) are assessed as a function of attrition time. Small angle X-ray scattering results show quantitatively that the number density of precipitated oxides increases as a function of milling time. This difference in oxide density alone is not enough to describe the tensile behavior of the NFA as a function of temperature. As a result, a previously proposed root mean square strengthening model is applied to the current study where direct dispersion strengthening, grain boundary strengthening, dislocation forest hardening, and matrix hardening are all considered. When an optimization routine is conducted, the fitting results suggest that the precipitated oxides are soft obstacles to dislocation motion.

DOI: 10.1007/s11661-014-2521-9

© The Minerals, Metals & Materials Society and ASM International 2014

I. INTRODUCTION

NANOSTRUCTURED ferritic alloys (NFAs) have seen a tremendous amount of work over the last decade for their potential applications in the nuclear power industry as an irradiation damage resistant material.^[1–5] This high irradiation damage resistance is a result of a dense dispersion of sub 10 nm oxides (NFs) that result from high energy milling, or attrition, processing. This processing step is critical to achieving both the desired irradiation damage resistance as well as the required structural properties.

It has been shown experimentally that well-processed NFAs result in the full dissolution of the starting yttrium oxide into the metal matrix during high energy attrition.^[1,6,7] Upon hot consolidation, complex oxides comprising titanium from the matrix as well as yttrium and oxygen, precipitate intra- and inter-granularly. This precipitation creates a homogeneous dispersion strengthening network and sets NFAs apart from conventional oxide dispersion strengthened (ODS) steels where full dissolution of the initial oxide does not occur. As a result, conventional ODS materials typically feature coarser oxides that exist more predominantly on grain boundaries or prior particle boundaries.^[8–10] These differences in oxide character and location result in reduced mechanical properties for conventional ODS materials when compared to NFAs.^[1,4,11]

Given the importance of attrition on the final NFA properties, this study seeks to isolate this variable and quantitatively assess the effects of attrition time on NF distribution and tensile properties. Identical consolida-

tion processing was used to produce NFA forgings of varying milling times. Milling trials and tensile tests were repeated to build statistical confidence for differentiation. The measured mechanical property differences are related to the microstructure through scanning electron microscopy (SEM), transmission electron microscopy (TEM), and small angle X-ray scattering (SAXS) characterization. A model for tensile yield strength based on the experimentally determined microstructural features is then applied, enabling strengthening mechanisms to be ascertained.

II. EXPERIMENTAL PROCEDURES

The NFA used for this study has a nominal composition in weight percent of Fe-14Cr-3W-0.4Ti-0.25Y₂O₃. The ferritic matrix powder (Fe-14Cr-3W-0.4Ti) was argon gas atomized by Carpenter and sieved to a mesh size of –150/+325 prior to attrition. The Y₂O₃ powder used was purchased from Alfa Aesar and had a quoted D₅₀ of 1.2 μm. A particle size distribution showed that the primary particle size was 1 μm while most particles were weak, 10 μm agglomerates following ultrasonication.

A. Processing

The attrition for all trials with Y₂O₃ was carried out by Zoz GmbH in a CM-20 mill at their facility in Wenden, Germany. The CM-20 mill was loaded with 3 kg of prealloyed and Y₂O₃ powder and a 30 kg charge of 100Cr6 milling media. Milling occurred under argon and no de-agglomerate aid was added. Milling conditions were held constant for all CM-20 trials with rotational speeds alternating between 200 and 450 rpm in 30 s intervals and milling times were varied between 4 and 40 h. An additional milling trial (Baseline-20) that excluded the addition of Y₂O₃ was done in a smaller,

RICHARD DIDOMIZIO, SHENYAN HUANG, LAURA DIAL, and MIKE LARSEN, Staff Scientists, are with GE Global Research, Niskayuna, NY 12309. Contact e-mail: didomizr@crd.ge.com JAN ILAVSKY, Scientist, is with the Argonne National Laboratory, Argonne, IL 60439.

Manuscript submitted December 10, 2013.

Article published online August 27, 2014

Table I. Milling Details for NFA and Baseline Samples

Sample Name	Mill	Mill Run Time (h)
NFA-4	CM-20	4
NFA-20A	CM-20	20
NFA-20B	CM-20	20
NFA-40	CM-20	40
Baseline-20	CM-01	20

NFA samples were milled in 3 kg batches in a larger Zoz mill for milling times varying from 4 to 40 h. Baseline was milled in 150 g batches in a smaller Zoz mill with speeds altered to match the kinetic energy input of the NFA runs.

Zoz CM-01 mill at GE Global Research. The milling speeds in the CM-01 were changed in order to approximate the kinetic energy achieved in the larger mill. Table I shows the lot name, milling time, and Zoz mill used for the five lots of powder that were investigated.

The milling times sampled cover a significant range of those reported in the literature, which can extend up to 80 h. However, it is not possible to directly compare milling times to those reported in the literature, as the kinetic energy imparted to the powder is a function of mill size, mill speed, and powder/milling media ratio. Following attrition, the powder was discharged into containers under inert gas. The inert gas cover was preserved by packing as-milled powders into hot isostatic pressing (HIP) cans in an argon-filled glovebox. The HIP cans were evacuated and degassed at room temperature and then at elevated temperature before being sealed and HIPed for 4 hours at 1200 K (927 °C) and 207 MPa.^[12] Following HIP consolidation, the 5 billets were then forged at identical conditions. Forging was completed to 75 pct engineering strain at 1200 K (927 °C) on an open die press controlled at a displacement rate of 1 mm/s.^[12] The forging platens were heated to 1173 K (900 °C) during forging to reduce billet cooling during the forging operation.

A small amount of as-milled powder was removed and air exposed for chemical analysis. Interstitial elements were measured *via* combustion infrared detection or inert gas fusion according to ASTM E1019-11. All other elements were measured *via* direct current plasma emission spectroscopy according to ASTM E1097-12. A scan was done for trace elements, and all elements that exist in excess of 0.01 wt pct are reported.

B. Tensile Tests

Buttonhead tensile bars were extracted perpendicularly to the forging direction. The straight section gage length was 9 mm and the gage diameter was 2.5 mm. Tensile tests were conducted on a closed loop servo controlled hydraulic test frame at a constant displacement rate of 0.0085 mm/s. The elevated temperature samples were heated in a resistive furnace and soaked for 10 min at the test temperature prior to beginning the test. An extensometer was not used and the final reported yield strength values are corrected for machine compliance.

C. Microscopy

High resolution backscattered electron (BSE) imaging was performed with a Hitachi SU70 FEG-SEM. Images were acquired with an yttrium-aluminum garnet (YAG) scintillator detector. The high sensitivity of this detector enables imaging with a relatively low beam current to improve resolution without compromising signal. Accelerating voltages ranged from 10 to 15 kV. Lower voltages were used to reduce the beam-sample interaction volume in an attempt to increase spatial resolution for imaging ultrafine grains in BSE mode. Transmission electron microscopy analysis was performed using a Tecnai F20 S/TEM with a Thermo NSS EDS system and a Tecnai Osiris S/TEM with high brightness X-FEG electron source and integrated Super-X EDS system plus an integrated FS-1 EELS spectrometer. Both field emission microscopes were operated at 200 kV. An on-axis BF/DF detector was used for STEM imaging. Phase contrast atomic resolution TEM images were captured with a bottom-mounted Orius camera and converted to FFT's using Gatan DigitalMicrograph.

Grain size determination for each milling time sample was made using five high-resolution BSE images taken from randomly selected areas within the metallographic mount. The magnification was selected to allow both the fine- and coarse-grains to be rated on the same image. A circle was digitally imposed on the microstructure and intersections were counted and converted to a grain size. The variation in grain size resulted in a lower than typical magnification which, in turn, resulted in a larger number of intersections than recommended by ASTM standards.

D. Small Angle X-ray Scattering (SAXS)

Thin slices for SAXS experiments were cut from the buttonheads of selected tensile specimens. The slices were further ground into thin foils with a thickness of 25 to 50 μm . Room temperature SAXS measurements were conducted at beamline 15-ID-D at the Advanced Photon Source, at Argonne National Laboratory. The X-ray energy was tuned to 30 keV with a sample-to-detector distance of 1.8 m, which covers a Q range of 0.02 to 0.7/ \AA . Measuring up to 0.7/ \AA is necessary to ensure that the flat background is well captured for accurate determination of the nanofeature (NF) volume fraction. A 200 \times 200 μm^2 beam was utilized, which provides good statistics on the ultrafine NFs. Eight random spots on each sample were measured to evaluate the microstructure homogeneity within a single sample. Specimens taken from duplicate tensile bars were measured to evaluate the microstructural difference among tensile bars extracted from different locations of the forging. The local sample thickness at the detected spots was derived from the measured transmission and the calculated linear absorption coefficient. This allowed scattering data to be reduced to absolute intensity scale *via* the Nika macro based on the measured glassy carbon standard for absolute intensity correction, silver behenate standard for sample-to-detector distance correction, dark current for transmission, and empty for

Table II. Chemical Analysis of As-milled Powder Lots in Weight Percent

Sample	Fe	O	N	C	Cr	W	Ti	Y	Si	Mn	Ni	Cu
NFA-4	bal.	0.17	0.01	0.03	13.6	3.2	0.34	0.22	0.44	0.37	0.02	0.04
NFA-20A	bal.	0.10	0.01	0.02	13.6	3.1	0.32	0.21	0.40	0.37	0.04	0.03
NFA-20B	bal.	0.09	0.01	0.02	13.8	3.2	0.31	0.20	0.39	0.35	0.02	0.04
NFA-40	bal.	0.10	0.02	0.04	14.0	3.1	0.36	0.19	0.35	0.37	0.04	—
Baseline-20	bal	0.01	<0.01	0.01	13.3	2.9	0.35	—	0.37	0.34	—	—

The first four samples had Y_2O_3 included in the mill during attrition. The fifth lot was milled without the inclusion of Y_2O_3 . The oxygen levels reported include oxygen in excess to that added through Y_2O_3 .

scattering from scotch tape.^[13] Quantitative analysis of NF size distribution and volume distribution was performed on the absolute intensity spectra using the maximum entropy method built in the Irena macro.^[14,15] Detailed descriptions of this methodology were reported elsewhere.^[16,17]

The absolute scattering intensity is a function of scatter morphology, size distribution, number density (or volume fraction), scattering length difference, or scattering contrast governed by chemistry of matrix and scattering particles, and is given by

$$I(Q) = |\Delta\rho|^2 \sum_{r_{\min}}^{r_{\max}} |F(Q, r)|^2 V^2(r) NP(r) \Delta r \quad [1]$$

where Q is the scattering vector, r is the characteristic length (radius for spherical particles), $\Delta\rho$ is the scattering contrast, $F(Q, r)$ is the scattering form factor for a single particle determined by morphology, $V(r)$ is the particle volume, N is the total number of scattering particles, and $P(r)$ is the probability of occurrence of particle at size of r . Equation [1] assumes that there are no interparticle interference effects. The maximum entropy method generates a histogram size distribution with a defined range of particle size and a fixed number of bins, as a solution to Eq. [1]. There is no assumption of the functional form of the size distribution (*i.e.*, Gaussian or log normal). Particles within the fitting size range are assumed to have the same scattering contrast and morphology. The scattering contrast between the Fe-14Cr-3W matrix and NFs used in the model fitting is $2.3 \times 10^{12}/\text{cm}^2$, based on the assumed NF chemistry of $Y_2Ti_2O_7$. This assumption is supported by TEM results in the current work and literature and is the same assumption that has been adopted by Olier *et al.*^[18] for small-angle neutron scattering (SANS) work completed on a similar NFA composition.

III. RESULTS

Chemistry analysis of the five lots of mechanically alloyed powder is shown in Table II. The consistent gas-atomized starting powder and the low major element contamination during milling result in excellent chemical uniformity across the five compositions. The oxygen levels reported in Table II are in excess to that added through Y_2O_3 . Thus, oxygen is incorporated into the

powder through both the milling process and the addition of Y_2O_3 .

The tensile results for all forgings are shown in Figure 1. The bars were not heat-treated prior to being tested as the HIP and forge consolidation path allowed for significant strain relief. The assessment of strain relief was based on the large drop in dislocation density from the as-milled powder to the as-consolidated powder seen in TEM, the minimal intragranular orientation contrast variation seen in BSE SEM, and the tested tensile ductility in excess of 10 pct even at room temperature. A room temperature ductility in excess of 10 pct is greater than that most often reported in the literature. Each NFA data point consists of a minimum of three individual tests. Where error bars are not seen, they are smaller than the marker size. All data points for the sample milled without Y_2O_3 (Baseline-20) are plotted.

The two individual 20 hour lots of NFA are grouped together as a single population because *t*-tests conducted at a 95 pct confidence level on the mean yield strength and plastic elongation to fail values showed that a statistically significant difference could not be found between the two lots at all test temperatures. An ANOVA analysis conducted at a 95 pct confidence level on the yield strengths for the three milling time populations at each of the temperatures indicates a significant difference is found. The larger scatter present in the plastic elongation to fail values results in no significant differences being found.

Figure 2 shows representative high resolution BSE SEM images of forged samples NFA-4, NFA-20B, and NFA-40, respectively. Micrographs are taken on a plane parallel to the forging direction. In the micrographs, color variation from grain to grain is due to differences in channeling contrast with crystallographic orientation, and not due to chemistry variation. Variations in contrast within a grain qualitatively indicate the level of retained strain.

It can be seen in Figures 2(a), (c), and (e) that all samples show a range of grain sizes. While the majority of grains are ultrafine grains with minimal retained strain, a distribution of larger, more highly strained, grains is present. The contrast in the large grains is continuous across the grains and does not change according to boundaries that could be associated with finer grains. A Monte Carlo simulation run in Casino V2.42 based on sample density and beam accelerating voltage shows that the electrons are not expected to

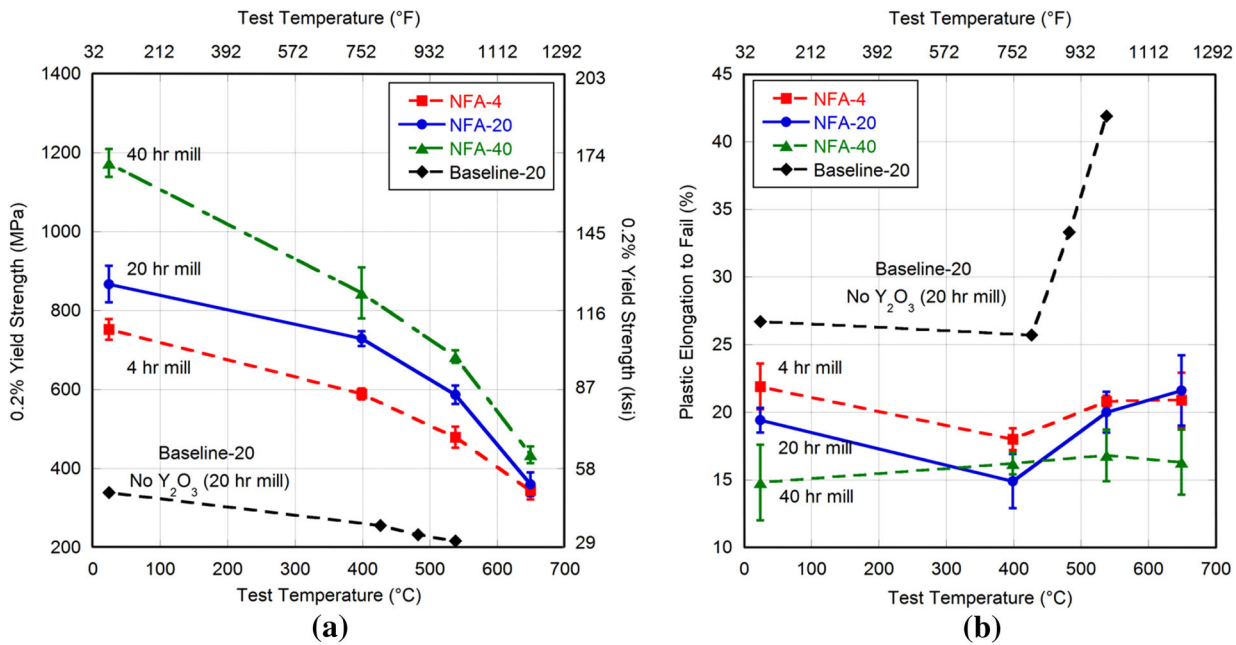


Fig. 1—Tensile (a) 0.2 pct yield stress data showing that increased milling time statistically increases the material yield strength and (b) plastic elongation to fail showing no statistically significant difference for compositions with Y₂O₃ included.

escape from a depth greater than 200 nm. This length is significantly less than the micron-sized large grains where the orientation contrast is most evident. Thus, the contrast within the large grains is attributed to the coarse grains and not sub-surface grains. The average grain size of each of the samples, taking into account all grain size populations is shown in Table III, as measured through the line intercept method discussed in Section II-C. The grain size of the sample milled without Y₂O₃, Baseline-20, is also shown for comparison.

Figures 2(b), (d), and (f), show a series of second phase particles decorating prior particle boundaries. Diffraction, electron energy loss spectroscopy (EELS), and EDS analysis (*via* TEM) show that these particles index to an MX, FCC structure, and they are rich in titanium, carbon, oxygen, and nitrogen. The interstitial elements (carbon, oxygen, nitrogen) were picked up during the milling process. These particles form during the elevated temperature consolidation of the powder and are similar to those that have been reported elsewhere.^[19]

TEM images of the NF distribution in samples NFA-4 and NFA-20B are seen in Figure 3. Sample NFA-4 shows an inhomogeneous distribution of NFs. As shown in Figure 3(a), alignment of NFs after forging was evident in some grains. Additionally, grains devoid of NFs were also routinely found. In contrast, Figure 3(b) shows a more homogenous distribution of NFs is present after 20 hour of milling (Sample NFA-20B). NFs were observed in all grains sampled. After 40 hour of milling (Sample NFA-40), a similar, homogenous distribution is observed, as compared to 20 hour of milling.

Insight into the NF character was obtained *via* TEM EDS on thin foils, extraction replicas, and TEM high-

resolution microscopy combined with Fast Fourier Transform (FFT) analysis. Figure 4 shows TEM EDS analysis conducted on an NF suspended above the thin foil hole to reduce matrix contributions. This analysis shows a roughly one-to-one yttrium-to-titanium atomic percentage ratio. Figure 5 shows a high-resolution TEM image of an NF sitting within the BCC ferritic steel matrix. The NF is crystalline and there are few, if any, misfit dislocations with the matrix indicating that the particle is incoherent with respect to the matrix. An FFT analysis of the NF atomic planes produces a pattern that matches a simulated diffraction pattern for stoichiometric Y₂Ti₂O₇. Additional high resolution TEM was performed on oxides as small as 4 nm in size. While an FFT analysis was not completed, the smaller oxides showed that they were also crystalline with no evidence of misfit dislocations at the oxide/matrix interface.

Despite experimental evidence to support an NF chemistry of Y₂Ti₂O₇, TEM EDS and FFT analysis could not definitively show that all particles analyzed were Y₂Ti₂O₇. The question of NF crystal structure and composition is still a highly debated topic in the literature. Williams *et al.*^[20] have provided a summary of the various NF oxides reported, including Y₂Ti₂O₇, Y₂TiO₅, YTiO₃, or a mixture of these oxides. In addition to the various oxides cited by William *et al.*, Hirata *et al.* have reported that the NFs in 14YWT are titanium-yttrium oxy-nitrides.^[21]

Quantitative analysis of the NF distribution in these samples is made *via* small angle X-ray scattering (SAXS) analysis. Given the uncertainty in exact NF character, this work uses the scattering contrast between the Fe-14Cr-3W matrix and an assumed stoichiometric Y₂Ti₂O₇ NF based on the above TEM results that support Y₂Ti₂O₇. Prior to analyzing the SAXS results as a function of milling time, several experiments were performed to

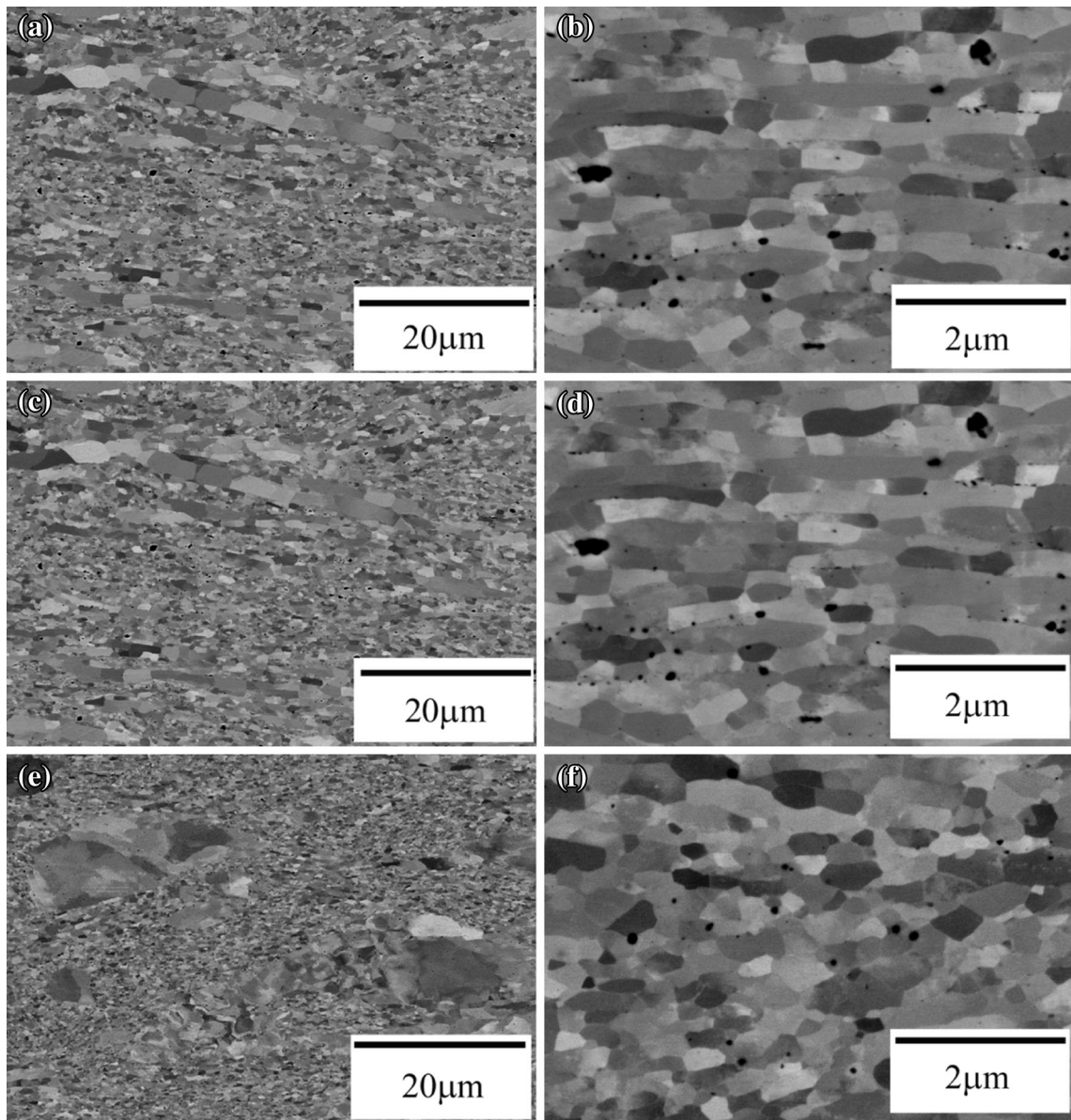


Fig. 2—BSE SEM images of the NFA milled for 4 h (a, b) 20 h (c, d), and 40 h (e, f).

Table III. Grain Size Values for All Milling Conditions

Sample	Average Grain Size (μm)	Grain Size Standard Deviation (μm)
NFA-4	0.9	0.1
NFA-20A	0.6	0.2
NFA-40	0.5	0.1
Baseline-20	3.6	0.5

Grain sizes were obtained from five different images for each milling condition.

assess variability. The variability in scattering intensity for a single location, when measured multiple times, was shown to be negligible in prior work. As a result, only multiple locations on multiple foils were measured to

assess variability. An example of this is shown in Figure 6 where eight distinct locations on a 40 hour milled sample were measured. The resulting absolute scattering spectra show minimal variation indicating that there is a homogeneous NF distribution on this length scale.

The SAXS scattering intensity spectra for NFA alloys milled for 4, 20, and 40 hour are presented in Figure 7(a), in addition to the alloy milled without Y_2O_3 . The power law slope at high Q is caused by particle scattering from grain boundaries, while the scattering intensity beyond this slope at high Q is caused by NFs. With the presence of Y-Ti-O NFs, NFA-4, NFA-20, and NFA-40 alloys, all show much higher scattering intensity compared to the baseline alloy containing no NFs. As milling time increases, the scattering intensity grows in the Q range of 0.05 to 0.3/ \AA , which indicates an increased number density of NFs.

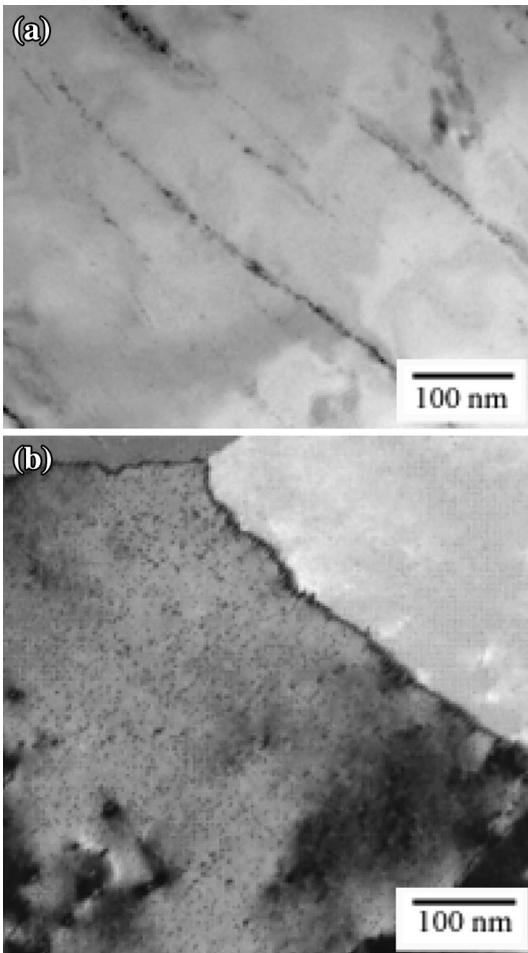


Fig. 3—Bright field STEM images showing NF distribution in (a) NFA-4 and (b) NFA-40. The NF distribution after 4 h of milling is inhomogeneous, with large areas of no precipitation. Milling for 20 and 40 h results in a homogeneous distribution.

With the assumption of the stoichiometric $Y_2Ti_2O_7$ NF chemistry and the experimentally measured scattering contrast, the size and volume distribution of NFs are obtained from model fitting, as shown in Figure 7(b). It is evident that the NF size decreases slightly and the NF volume fraction increases dramatically as milling time increases. A bimodal or trimodal size distribution is found for each milling time with the majority of NFs having a diameter below five nm. The volume fraction and number density of NFs reported here are integrated within the diameter range of one to five nm. Additional GE Global Research TEM results demonstrate that sub 5 nm NFs act as strong pinning sites for dislocation motion agreeing with previous reports.^[22] Thus, integrating over the 1 to 5 nm particle range captures the microstructural features driving the material response.

By comparing the SAXS scattering curves and NF size distribution results, the microstructural variability at different locations within each specimen has been evaluated for all the samples. Table IV summarizes the average, standard deviation, minimum, and maximum values for NF volume fraction and number density among eight measured spots. Paired *t* tests and an

ANOVA analysis indicate that when a 90 pct confidence interval is considered, there is no statistically significant difference seen in (1) tensile bars extracted from the same forged lot and (2) materials from NFA-20A and NFA-20B.

IV. DISCUSSION

The tensile yield strengths achieved by NFAs are a combination of several strengthening mechanisms including direct dispersion strengthening (σ_D), grain boundary strengthening (σ_k), dislocation forest hardening (σ_ρ), and matrix hardening (σ_m). Kim *et al.*^[23] have recently proposed a root mean square (RMS) summation model for the superposition of these mechanisms to predict the tensile strengths of several dispersion strengthened materials, including the NFA 14YWT having a uniform grain size and NF density. The NFA in the current study is compositionally very similar to the 14YWT NFA studied by Kim *et al.* However, the consolidation practice in the current work is different.

$$\Delta\sigma_{rms} = \sqrt{(\sigma_\rho^2 + (\sigma_D + \sigma_k + \sigma_m)^2)} \quad [2]$$

Unlike a linear superposition model, the RMS model takes into account the high probability of interacting mechanisms given the common underlying dislocation motion and interaction mechanisms that are active in NFAs.

While many model parameters were taken directly from Kim *et al.* and applied to the current NFA, both the NFA microstructures and tensile properties shown in the current work are significantly different than those reported by Kim *et al.* Kim *et al.* report a uniform grain size of approximately 200 nm and a maximum assumed NF number density of $4 \times 10^{23} \text{ 1/m}^3$. This resulted in a room temperature tensile strength of approximately 1600 MPa and a strain to fail of approximately 3 to 4 pct.^[24] In the current work, the 4 hour milled sample (14YWT-4) has an average NF number density of $3.63 \times 10^{23} \text{ 1/m}^3$ inhomogeneously dispersed with a wide grain size distribution and a mean grain size of 900 nm. This results in a room temperature strength of approximately 800 MPa, but a plastic strain to fail value in excess of 20 pct. Thus, microstructural differences lead to significant changes in bulk tensile properties. Given the differences in properties, grain size, and measured NF number density seen in the current NFA alloy, Kim *et al.*'s model is applied to this material to understand how the four defined strengthening mechanisms are interacting.

The dispersion strengthening behavior was evaluated for both an Orowan mechanism, in which NFs act as hard, impenetrable barriers to dislocation motion and a dispersed barrier hardening model, in which the NFs are shearable by propagating dislocations.^[25,26] The Orowan mechanism is not fully discussed as the resulting predictions are significantly higher than the experimental data, as also reported by Kim *et al.* In addition, there is no TEM evidence of NFs being surrounded by dislocation loops to indicate an Orowan mechanism is taking place.

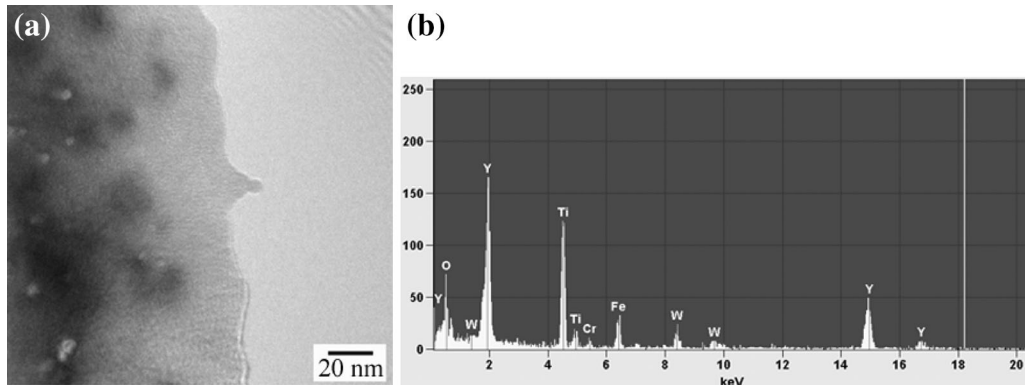


Fig. 4—(a) TEM bright-field image showing a nanofeature protruding into the hole of a thin foil sample. (b) EDS from this nanofeature with minimal matrix contribution.

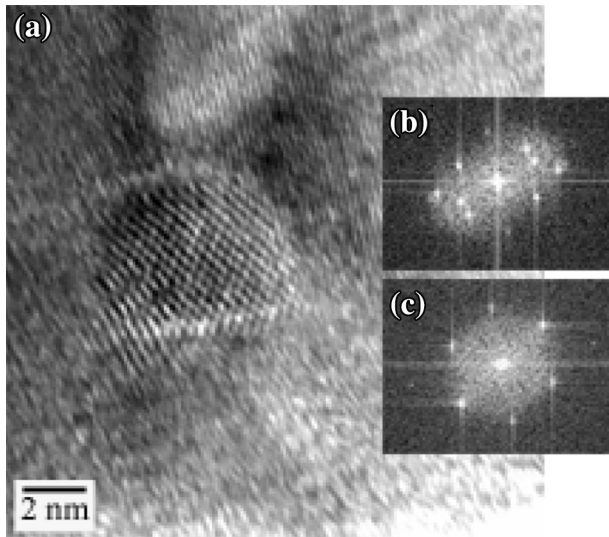


Fig. 5—(a) Atomic resolution TEM image of a nanofeature. The FFT from the nanofeature (b) was analyzed using a matrix FFT (c) as an internal standard. The nanofeature FFT matches the simulated (110) zone axis diffraction pattern for $Y_2Ti_2O_7$.

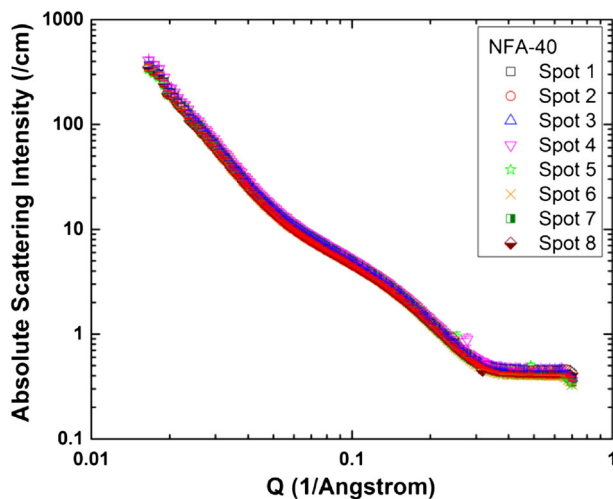


Fig. 6—Absolute scattering spectra of NFA-40 measured at eight distinct locations randomly selected on a single SAXS sample. The results show nanofeature homogeneity within one sample.

The dispersed barrier approach is described by

$$\Delta\sigma_{dbh} = \frac{0.8M\alpha(r)Gb}{\lambda} \quad [3]$$

$$\alpha(r) = 0.27 \log\left(\frac{r}{2b}\right) \quad [4]$$

where M is the Taylor factor (2.7), G is the shear modulus, b is the burgers vector (0.2474 nm), and λ is the mean planar interparticle spacing. The shear modulus was calculated as a function of temperature based on the experimentally measured dynamic modulus determined by sonic resonance (ASTM E1875) and an assumed Poisson's ratio as shown in Table V.^[27] The shear modulus is the only temperature dependent term for the direct dispersion hardening term. The burgers vector is kept constant because the effect of the coefficient of thermal expansion is minimal. The interparticle spacing was determined according to Sekido *et al.*^[28] and used the SAXS determined NF diameters and volume fractions. The $\alpha(r)$ parameter is a barrier strength coefficient that is intended to represent the strength of the NFs. Alinger *et al.* showed *via* interpolation that Eq. [4] provided a good fit to the available NFA experimental data and this results in an $\alpha(r)$ equal to 0.13 for the NFA in the present work.^[1] This is slightly lower than the value used by Kim *et al.* and indicates that the current work is treating the NFs as even softer particles.

The grain boundary strengthening component of the overall strength is provided *via* Hall-Petch strengthening.^[24] Because the current work has a convolution of grain size and nanofeature density changes, the Hall-Petch parameters were taken directly from Kim *et al.* as a function of temperature. As a result, the same decrease in yield strength is predicted above 227 K (500 °C) due to a drop in the Hall-Petch parameter.

The dislocation forest hardening strengthening component is given by

$$\sigma_\rho = M\gamma Gb\sqrt{\rho} \quad [5]$$

where ρ is the dislocation density and γ is a material-dependent constant. While Kim *et al.* used a γ value of 0.38, the current work uses a value of 0.27. This value

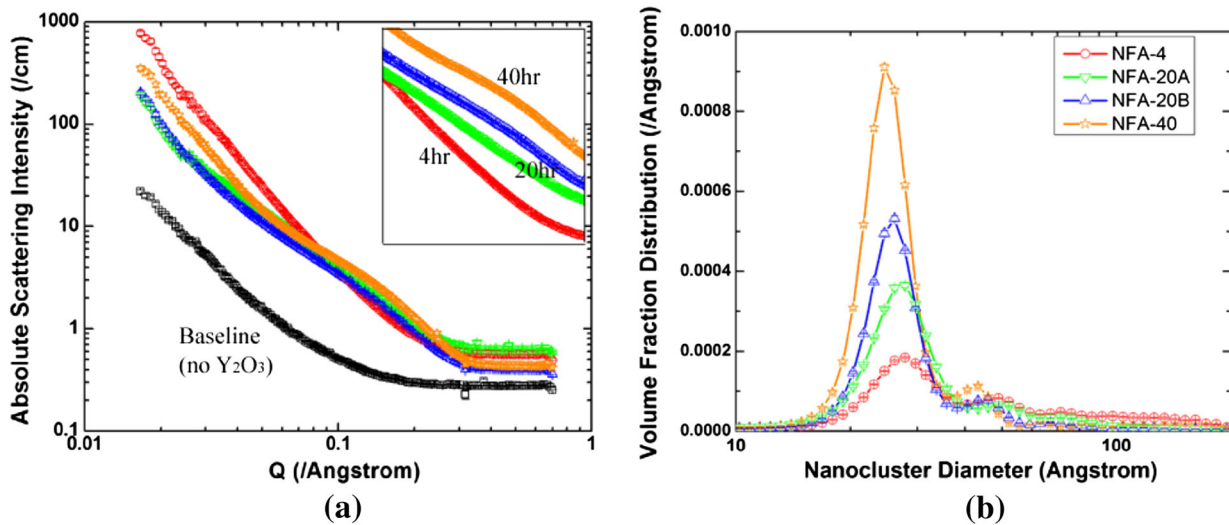


Fig. 7—(a) Absolute scattering spectra of 4, 20, and 40 h milled alloys compared to NFA-20. Data in the Q range of 0.05 to $0.3/\text{\AA}$ are vertically adjusted to show curvature and magnified in the insert figure to emphasize the trend. (b) Volume distribution as a function of size distribution obtained from model fitting.

Table IV. Fitting Results of SAXS Specimens Including Average Value, Standard Deviation (STD), Minimum Value and Maximum Value of Nanofeature Volume Fraction and Number Density (ND)

Sample Name	Avg (vol. pct)	SD (vol. pct)	Min (vol. pct)	Max (vol. pct)	Avg ND ($1/\text{m}^3$)	Std ND ($1/\text{m}^3$)	Min ND ($1/\text{m}^3$)	Max ND ($1/\text{m}^3$)
NFA-4	0.39	0.028	0.34	0.43	3.6×10^{23}	4.9×10^{22}	2.7×10^{23}	4.2×10^{23}
NFA-20A	0.58	0.052	0.53	0.68	6.7×10^{23}	8.6×10^{22}	5.6×10^{23}	8.3×10^{23}
NFA-20B	0.64	0.049	0.60	0.74	7.2×10^{23}	4.0×10^{22}	6.6×10^{23}	7.8×10^{23}
NFA-40	0.97	0.028	0.93	1.01	1.3×10^{24}	9.3×10^{22}	1.1×10^{24}	1.4×10^{24}

The number density of nanofeatures increases as a function of milling time.

Table V. Calculated Values for Young's Modulus and Shear Modulus Obtained from Experimental Longitudinal Velocity Measurements

Temperature [K (°C)]	Assumed Poissons	Youngs Modulus (GPa)	Shear Modulus (GPa)
297.1 (23.9)	0.28	229.2	89.5
477.6 (204.4)	0.29	211.1	81.8
699.9 (426.7)	0.30	189.1	72.7
755.4 (482.2)	0.30	181.9	70.0
811.0 (537.8)	0.31	173.0	66.0
866.5 (593.3)	0.31	171.2	65.4
922.1 (648.9)	0.31	169.3	64.6

was chosen based on the dislocation densities utilized by Kim *et al.* in his work which have units of m/m^3 . Dislocation densities measured as a length per volume have roughly twice the density reported for dislocation densities reported as intersection per unit area. As a result, the γ value is a factor of approximately 1.4 higher.^[29] The current work initially uses the dislocation densities reported by Kim *et al.* with no changes as a result of increasing NF density.

The grain matrix hardening as a function of temperature was also taken directly from Kim *et al.* While the current work did complete a set of experiments without oxides present, the material was milled prior to consolidation resulting in a finer grain size. Thus, the Hall-

Petch component cannot be completely ignored from the current work's resulting strength.

Figure 8(a) shows the RMS strength model predictions compared with the experimental data. At the four temperatures where there is experimental data, scatter bands have been plotted for the RMS model prediction. These scatter bands are the result of predictions covering the grain size standard deviation measured. In general, the model correctly predicts the strength change that results from the change in grain size and NF density as a function of milling time and test temperature. However, the strength model over predicts the strength for the 4 and 20 hour milling trials over the entire temperature range, even when considering the scatter

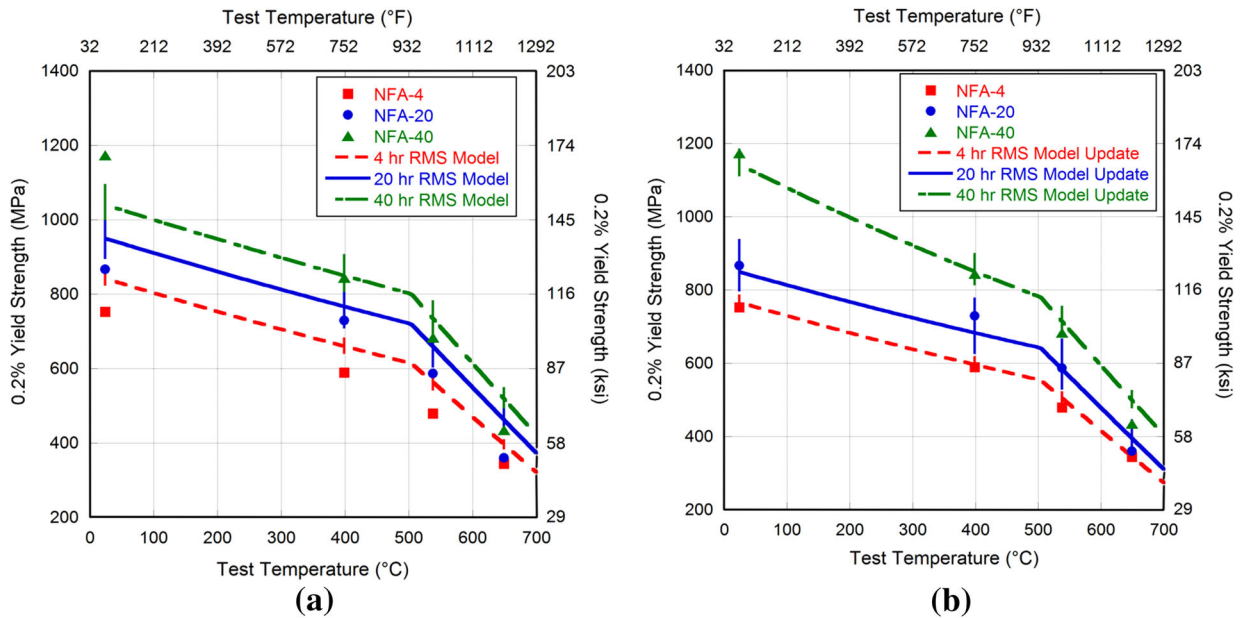


Fig. 8—The root mean square tensile model using (a) initial parameters generally exhibits the correct curve shape to approximate the experimental result, though good agreement is not reached. When an optimization routine on several uncertain parameters is performed, the tensile model (b) better matches the experimental result.

due to the grain size variation. The model does a better job predicting the high temperature 40 hour experimental data, but is unable to provide a good prediction at room temperature. This change in predictability seen only across the 40 hour temperature range suggests that a material parameter that has been held constant across all three milling times is not correct and should vary as a function of milling time. When the TEM micrographs of the 4, 20, and 40 hour milling trials are examined, it qualitatively appears that there is greater retained strain, and thus a greater dislocation density present following the 40 hour milling cycle. This is reasonable as there is more strain energy in the powder and there is a greater density of NFs to trap dislocations during the consolidation process. A quantitative assessment of dislocation density was not made.

In order to obtain a better fit between the model and experimental data, $\alpha(r)$ for all milling times and a coefficient on Kim *et al.*'s reported dislocation density values for the 40 hour trial were allowed to vary. The square root of the sum of the squares of the residuals was calculated and an optimization routine was run to minimize this value. This resulted in an $\alpha(r)$ value of 0.056 and a 40 hour dislocation density increase of 3.3 over what is used for the 4 and 20 hour milling trials. The fit $\alpha(r)$ value is lower than the value used by Kim *et al.* and Alinger *et al.*; however, it is still in the range considered to be reasonable.^[1,23] The new model results are shown in Figure 8(b) and they show a better fit to the experimental data. The updated model results suggest that the NFs are softer obstacles than what is reported by previous authors. This would indicate that the NFs are shearable. To date, however, TEM micrographs have not shown any definitive evidence of sheared NFs in strained materials.

V. CONCLUSIONS

The tensile properties of a 14Cr NFA are directly associated with the microstructural variations that arise from attrition processing changes. Attrition times that are too short result in an under-milled condition, whereby the NF distribution is inhomogeneous. Longer milling times result in more homogeneous NF distribution and an increasing density of NFs as quantified by SAXS analysis. The quantified change in NF density alone is not enough to fully describe the change in NFA tensile strength as function of temperature. Grain boundary strengthening, dislocation forest hardening, and matrix hardening all need to be considered. Based on the currently described root mean square strength model, NFs need to be considered as “soft” particles to achieve the best fit with experimental data. Further TEM investigations are needed to assess whether this is correct.

ACKNOWLEDGMENTS

This material is based upon work supported by the Department of Energy under Award Number EE0003487. This report was prepared as an account of work sponsored by an agency of the United States Government. Neither the United States Government nor any agency thereof, nor any of their employees, makes any warranty, express or implied, or assumes and legal liability or responsibility for the accuracy, completeness, or usefulness of any information, apparatus, product, or process disclosed, or represents that its use would not infringe privately owned rights. Reference herein to any specific commercial product,

process, or service by trade name, trademark, manufacturer, or otherwise does not necessarily constitute or imply its endorsement, recommendation, or favoring by the United States Government or any agency thereof. The views and opinions of authors expressed herein do not necessarily state or reflect those of the United States Government or any agency thereof. ChemMatCARS Sector 15 is principally supported by the National Science Foundation/Department of Energy under grant number NSF/CHE-0822838. Use of the Advanced Photon Source, an Office of Science User Facility operated for the U.S. Department of Energy (DoE) Office of Science by Argonne National Laboratory, was supported by the U.S. DoE under Contract No. DE-AC02-06CH11357. The authors greatly acknowledge Dr. Matthew Alinger, Dr. Ernie Hall, Dr. Yan Gao, Mr. Orrie Riccobono, Mr. Ian Spinelli, Mr. Tony Barbuto, Ms. Rebecca Casey, Mr. Mitchell Hammond, and Dr. Ning Zhou for their efforts and discussions.

REFERENCES

1. G.R. Odette, M.J. Alinger, and B.D. Wirth: *Ann. Rev. Mater. Res.*, 2008, vol. 38, pp. 471–503.
2. N. Akasaka, S. Yamashita, T. Yoshitake, S. Ukai, and A. Kimura: *J. Nucl. Mater.*, 2004, vols. 329–333, pp. 1053–56.
3. A. Alamo, V. Lambard, X. Avery, and M.H. Mathon: *J. Nucl. Mater.*, 2004, vols. 329–333, pp. 333–37.
4. G.R. Odette and D.T. Hoelzer: *JOM*, 2010, vol. 62, pp. 84–92.
5. P.D. Edmondson, C.M. Parish, Y. Zhang, A. Hallen, and M.K. Miller: *Scripta Mater.*, 2011, vol. 65, pp. 731–34.
6. M.J. Alinger: Ph.D Thesis, University of California, Santa Barbara, 2004.
7. Y. Kimura, S. Takaki, S. Suejima, R. Uemori, and H. Tamehiro: *ISIJ Int.*, 1999, vol. 39, pp. 176–82.
8. G.S. Ansell, T.D. Cooper, and F.V. Lenel: *Oxide Dispersions Strengthening*, Gordon and Breach, New York, 1968.
9. M. Hasegawa and M. Osawa: *Metall. Trans. A*, 1985, vol. 16A, pp. 1043–48.
10. D. Haussler, B. Reppich, M. Bartsch, and U. Messerschmidt: *Mater. Sci. Eng. A*, 2001, vols. 309–310, pp. 500–04.
11. T. Hayashi, P.M. Sarosi, J.H. Schneibel, and M.J. Mills: *Acta Mater.*, 2008, vol. 56, pp. 1407–16.
12. R. DiDomizio, M. Alinger, R. Stonitsch, and S. Thamboo: US patent 8,357,328 (2013).
13. J. Ilavsky: *J. Appl. Cryst.*, 2012, vol. 45, pp. 324–28.
14. J. Ilavsky and P.R. Jemian: *J. Appl. Cryst.*, 2009, vol. 42, pp. 347–53.
15. P.R. Jemian, J.R. Weertman, G.G. Long, and R.D. Spal: *Acta Metall. Mater.*, 1991, vol. 39, pp. 2477–87.
16. J.A. Potton, G.J. Daniell, and B.D. Rainford: *J. Appl. Cryst.*, 1988, vol. 21, pp. 663–68.
17. J.A. Potton, G.J. Daniell, and B.D. Rainford: *J. Appl. Cryst.*, 1988, vol. 21, pp. 891–97.
18. P. Olier, J. Malaplate, M.H. Mathon, D. Nunes, D. Hamon, L. Touabli, Y. de Carlan, and L. Chaffron: *J. Nucl. Mater.*, 2012, vol. 428, pp. 40–46.
19. P. Olier, M. Couvart, C. Cayron, N. Lochet, and L. Chaffron: *J. Nucl. Mater.*, 2013, vol. 442, pp. S106–11.
20. C.A. Williams, P. Unifantowicz, N. Baluc, G.D. Smith, and E.A. Marquis: *Acta Mater.*, 2013, vol. 61, pp. 2219–35.
21. A. Hirata, T. Fujita, C.T. Liu, and M.W. Chen: *Acta Mater.*, 2012, vol. 60, pp. 5686–96.
22. M. Brandes, L. Kovarik, M. Miller, G. Daehn, and M. Mills: *Acta Mater.*, 2011, vol. 60, pp. 1827–39.
23. J. Kim, T. Byun, D. Hoelzer, C. Park, J. Yeom, and J. Hong: *Mater. Sci. Eng. A*, 2013, vol. 559, pp. 111–18.
24. J. Kim, T. Byun, D. Hoelzer, S. Kim, and B. Lee: *Mater. Sci. Eng. A*, 2013, vol. 559, pp. 101–10.
25. G. Dieter: *Mechanical Metallurgy*, McGraw Hill, Boston, 1986.
26. S. Zinkle and Y. Matsukawa: *J. Nucl. Mater.*, 2004, vols. 329–333, pp. 88–96.
27. G. Blessing: in *Dynamics Elastic Modulus Measurements, ASTM STP 1045*, A. Wolfenden, ed., American Society for Testing and Materials, Philadelphia, PA, 1990, pp. 47–57.
28. Z. Sekido, A. Hoshino, M. Fukuzaki, Y. Mitarai, and T. Maruko: *Mater. Sci. Eng. A*, 2011, vol. 528, pp. 8451–59.
29. M. Kassner: *Acta Mater.*, 2004, vol. 52, pp. 1–9.